Anisotropic gradients in Iran: Quasi-Love waves illuminate the deep structure and deformation style of the Zagros, Alborz, and Kopet Dagh

Amir Sadeghi-Bagherabadi [a,b,c,d,*], Lucia Margheriti [b], Abdelkrim Aoudia [c], Paola Baccheschi [b], Francesco Pio Lucente [b], Farhad Sobouti [d]

[a] Institute of Seismology, University of Helsinki, Helsinki, Finland
[b] Istituto Nazionale di Geofisica e Vulcanologia (INGV), Rome, Italy
[c] Earth System Physics Section, The Abdus Salam International Centre for Theoretical Physics (ICTP), Trieste, Italy
[d] Department of Earth Sciences, Institute for Advanced Studies in Basic Sciences (IASBS), Zanjan, Iran

A R T I C L E   I N F O

A B S T R A C T

We investigate the presence of the quasi-Love wave (qL) at 51 seismic stations of a temporary seismic network across the western Arabia-Eurasia collision zone. We quantify the intensity of the qL observations from the April 12, 2014 Solomon Islands earthquake by calculating the peak-to-peak amplitude ratios of the qL and Love waves, and compare them with predicted qL intensities from previous shear-wave splitting results. We determine the polarity, timing, and period-dependence of the qL observations within the period range of 50–100 s. Our analysis reveals that the qL observations at stations in the Zagros and Alborz mountain belts exhibit opposite characteristics. In contrast to the Alborz stations, the intensity of qL observations at the Zagros stations exhibits relatively negligible dependence on the period, while their receiver-scatterer distances are considerably period-dependent. We approximately locate the anisotropic gradients that generate the qL waves. Our results suggest that a lithospheric gap is responsible for the shallow and abrupt variation in the belt-parallel trend of fast-axis orientations in the westernmost part of the Zagros. Additionally, the period/depth dependence of the anisotropic gradients along the boundary between the central Zagros and central Iran provides insight into the variation in the downward dip of the Arabian lithosphere. The anisotropic gradient located to the north of the Doruneh fault in eastern Iran indicates its role as a major shear zone and lithospheric boundary. Finally, we observe that the spatial distribution of the anisotropic gradient in northeastern Iran matches the higher strain-rate areas in the Kopet Dagh Mountains, suggesting coupling between the lithospheric mantle and crust in that region.

1. Introduction

In order to comprehend the tectonic evolution of continental collision zones, it is essential to have a comprehensive understanding of the dynamics of deformation within both the lithosphere and asthenosphere. To this end, it is necessary to investigate the relationship between deformation and flow field at depth, and surface deformation inferred from geodetic velocity fields. Seismic anisotropy measurements can be utilized to determine the direction of flow and strain fields in the mantle and crust. The anisotropic structure of the Earth can be assessed by studying its effects on seismic waves. Analysis of shear-wave splitting is known to be a reliable detector of azimuthal anisotropy. The azimuthal dependence of the Pn velocities is another indicator. Seismic

anisotropy also affects surface waves through various mechanisms such as azimuthal variation of group and phase velocities, the discrepancies between Love and Rayleigh waves caused by vertical transverse isotropy, and generation of coupled-mode phases such as the quasi-Rayleigh and quasi-Love (qL) waves (Long and Becker, 2010).

The current geodynamic structure of the Iranian plateau is the product of the subduction of the Paleo-Tethys and the Neo-Tethys under Eurasia during the Mesozoic-early Cenozoic, followed by the collision of Arabia with Eurasia in the later part of the Cenozoic. The plateau comprises several principal tectonic blocks, including the Zagros active Fold-and-Thrust Belt (ZFTB) in the west and south, the Sanandaj-Sirjan Zone (SSZ) and Urmieh-Dokhtar Magmatic Arc (UDMA) regions, the Alborz and Kopet Dagh mountain ranges in the north, the central Iran

---

micro-continental blocks (CIMC), and the Makran subduction zone in the southeast (Fig. 1a). This assemblage has been accreted to the southern margins of Eurasia through an extended tectonic history.

Seismic imaging studies have revealed much detail of the structure of the continental collision of Arabia with Eurasia in Iran. Despite differences in the geodynamic interpretations, most studies have confirmed a thick (~250 km) high-velocity lithosphere beneath the Zagros, and a thinner lithosphere (~100 km) beneath central Iran (Fig. 1a). However, the variation of the geometry of the lithosphere-asthenosphere system along the strike of the Zagros remains uncertain.

Shad Manaman and Shomali (2010) and Shad Manaman et al. (2011) utilized the partitioned waveform inversion technique to study the S-wave and P-wave structure of the Zagros region down to 600 km depth. Shomali et al. (2011) employed non-linear teleseismic tomography for the same investigation. They postulated that lithospheric delamination has taken place beneath the eastern Zagros. Another proposed scenario is crustal underthrusting of Arabia beneath central Iran in the eastern Zagros, as suggested by Paul et al. (2006), Kaviani et al. (2007); Paul et al. (2010); Motaghi et al. (2015), and Pilia et al. (2020). Mohammadi et al. (2013) conducted a S receiver function study in order to detect deep discontinuities beneath the Zagros collision zone, which revealed the presence of a 200 km thick lithosphere. Seismic tomography studies (Hafkenscheid et al., 2006; Priestley et al., 2012; Mahmoodabadi et al., 2019) have revealed a deep high-velocity body beneath both eastern and western Zagros, which has been attributed to lithospheric thickening.

The western Zagros region remains understudied compared to the eastern Zagros, and the present lithospheric structure of the region is still the subject of debate. Although interpretations from a few seismic imaging studies focused on the western Zagros differ from one another, the majority of studies support the hypothesis of lithospheric thickening beneath the Zagros and the underthrusting of the Arabian lithosphere

beneath central Iran (Hafkenscheid et al., 2006; Paul et al., 2010; Priestley et al., 2012; Mohammadi et al., 2013; Motaghi et al., 2017; Mahmoodabadi et al., 2019; Dashti et al., 2020; Veisi et al., 2021; Irandoust et al., 2022). Some recent tomography results have raised the possibility of lithospheric delamination underneath the western Zagros. Rahmani et al. (2019) inverted regional and teleseismic P-wave relative time residuals to resolve the lithospheric structure beneath the western Zagros. They observed a low velocity wedge in the ~100–250 km depth range beneath the Zagros suture and interpreted it as a signature of delamination of the lower part of the Arabian lithosphere. Mahmoodabadi et al. (2020) employed a joint inversion technique using surface wave dispersion and teleseismic P-wave coda. They reported a narrow low-velocity corridor beneath the northern edge of the western Zagros, which they proposed was formed due to the peeling of the lithospheric mantle from the base of the overlying crust through the delamination process. Such a low-velocity feature is also observed by other regional studies (Movaghari and Doloei, 2020; Movaghari et al., 2021; Mohammadi et al., 2022). The most recent 3D teleseismic P-wave tomography of Veisi et al. (2021) covering the western Zagros clearly imaged the extent of the detached slab and the thickened root of the Zagros. Their tomographic images revealed that the depth of the top of the detached slab tends to increase from the western Zagros towards the central and eastern Zagros, suggesting that the detachment in the western Zagros is at an earlier stage. They also imaged a small-scale lateral lithospheric discontinuity along the Zagros and the lateral variation in the geometry of the Arabian lithosphere. The latter is also observed in the S-wave velocity model presented by Mohammadi et al. (2022).

The crustal and lithospheric structure of central Iran and Kopet Dagh have been recently investigated by seismic imaging and potential field studies. Motaghi et al. (2015) carried out a simultaneous inversion of receiver functions and Rayleigh wave group velocities and validated their results by modeling the Bouguer gravity anomaly data. Their
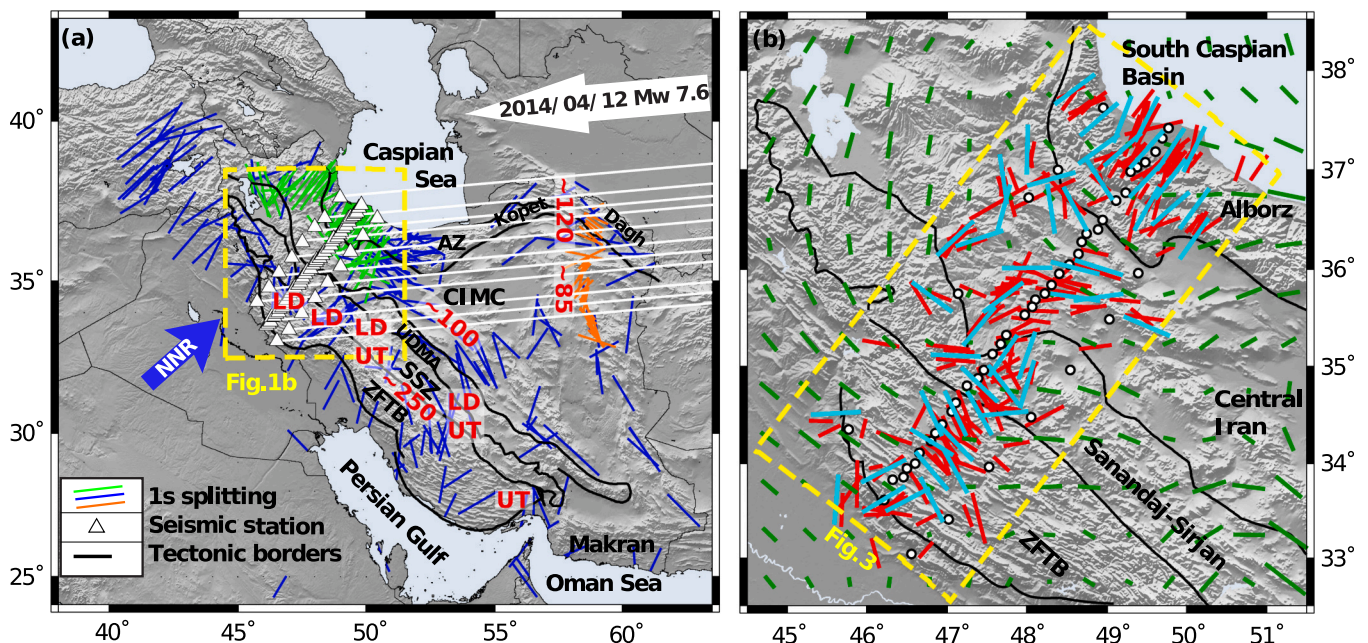

Fig. 1. (a) Map of the Arabia-Eurasia collision zone and the main tectonic provinces in the region. Back-azimuth of the April 12, 2014, Mw 7.6 Solomon Islands earthquake and the direction of plate motion in the no-net-rotation (NNR) reference frame are shown by white and blue thick arrows, respectively. The white lines represent the raypaths of the Solomon Islands earthquake. The yellow box area is the frame of the map in Fig. 1b. Splitting results of Arvin et al. (2021), Kaviani et al. (2021) and Gao et al. (2022) are shown by green, blue and orange bars, respectively. Approximate thickness of lithosphere in km and locations of the proposed underthrusting and lithospheric delamination are marked by red. Abbreviations are defined as follows: AZ, Alborz; ZFTB, Zagros Fold-and-Thrust Belt; SSZ, Sanandaj-Sirjan Zone; UDMA, Urmieh-Dokhtar Magmatic Arc; CIMC, Central Iran Micro-Continent; UT, underthrusting; LD, lithospheric delamination. (b) Map showing the temporary seismic network used in this study (circles). Red bars are the individual splitting results projected down to the 150 km depth piercing points from Sadeghi-Bagherabadi et al. (2018b). Cyan bars represent their averages over a regular grid. Dark green bars illustrate the Pn anisotropy measurements by Lü et al. (2017). The yellow box area is the frame of the map in Fig. 3.

tomographic image revealed a sub-crustal low-velocity body beneath the CIMC to the south of the Doruneh fault. Namvaran et al. (2020) imaged the same structure in their integrated potential field data modeling, which was found to be consistent with the larger-scale P-wave tomography of Wei et al. (2019). Wu et al. (2021) used the S receiver function data from a dense seismic array to construct a structural image of the lithosphere-asthenosphere system across the northeastern and eastern Iranian plateau. Their findings revealed that the lithosphere is 80–90 km thick in eastern Iran and tends to be thickened northward where it reaches ~120 km beneath the Kopeh Dagh.

Several studies on seismic anisotropy of the Arabia-Eurasia collision zone in Iran have been carried out in the recent past. Kaviani et al. (2021) performed a shear-wave splitting analysis on core-refracted phases at 226 permanent and temporary seismic stations throughout Iran, which was an expansion and reprocessing of data from an earlier study (Kaviani et al., 2009). In their map of splitting results, the eastern Zagros was represented by mostly NNW-SSE fast polarization directions (FPDs), while the central Alborz and Kopet Dagh were dominated by belt-parallel trends of the FPDs. In the northern margin of the Zagros their results showed NE-SW FPDs and they interpreted them as representative of a circular flow around a thick Zagros lithosphere. The SKS splitting study by Sadeghi-Bagherabadi et al. (2018a) utilized 63 temporary seismic stations of the CIGSIP network (Fig. 1) in the western Arabia-Eurasia collision zone and revealed a complicated pattern of station-averaged FPDs (Fig. 1b). They reported NW-SE and NE-SW FPDs in the western Zagros and western Alborz, respectively, while in central Iran yet another set of NW-SE and NE-SW trends prevails (Fig. 1b). Sadeghi-Bagherabadi et al. (2018b) investigated the individual splitting measurements obtained from the CIGSIP stations to detect anisotropic variations both along and across the collision zone, with the aim of determining their source layer. They discussed the depth dependence of anisotropy and the possibility of a layered anisotropic structure beneath the Arabia-Eurasia collision zone. They based their hypothesis on shear-wave splitting measurements and previous Pn anisotropy studies (Lü et al., 2017) and compared them with the absolute plate motion vectors (APM) (Fig. 1) to construct 2-D and 3-D geodynamical models of the region. Arvin et al. (2021) also performed shear-wave splitting analysis on the teleseismic SK(K)S and direct S wave recordings of 68 temporary stations in NW Iran. Their results were dominated by a uniform pattern of NE–SW FPDs. More recently Gao et al. (2022) analysed the core-refracted phases recorded by 65 seismic stations of a reverse-L shape seismic array in eastern Iran. Their shear-wave splitting results revealed small-scale variations in splitting parameters occurring at major tectonic boundaries in the region. They reported NW-SE FPDs in the eastern part of Kopet Dagh which are consistent with the results of Kaviani et al. (2021). They found NE-SW FPDs in the northern Lut block, but NNW-SSE directions in the vicinity of the northern Sistan suture zone.

In this study we use observations of the qL phases recorded by 63 seismic stations in western Iran as an alternative method for investigating azimuthal anisotropy beneath the Iranian plateau. Our approach involves quantifying the intensity of the observed quasi-Love waves and exploring their period dependence, polarization, and timing. Additionally, we estimate the approximate locations of the causative anisotropic gradients. We integrate our results with the recent findings from shear-wave splitting and seismic imaging studies to further our knowledge of the large-scale source regions and variations of anisotropy, and make inferences on the present state of the western Zagros lithosphere and the style of deformation in the collision zone.

2. Methods

Love and Rayleigh waves are commonly observed surface waves with significant amplitudes on horizontal and vertical components of seismograms, respectively. Love waves propagate faster than Rayleigh waves and therefore for long epicentral distances, the time windows of Love and Rayleigh wave trains are separated enough to allow for recognition of the different wave packets. Quasi-Love waves are infrequently observed coupled-mode phases that arise as a result of scattering from Earth's toroidal to spheroidal free oscillations. These waves manifest as anomalous phases within the Love wave time window, yet they exhibit substantial amplitudes on the vertical component and share polarizations similar to those of Rayleigh wave. Despite the rarity of qL observations, several previous studies have shown that their generation is due to the presence of azimuthal anisotropic gradients along raypaths rather than variations in the isotropic body wave velocities or the presence of radial anisotropy (one with a vertical symmetry axis) (Park and Yu, 1992; Yu and Park, 1993; Yu et al., 1995; Rieger and Park, 2010). The anisotropic gradient—specifically a change in anisotropy, either in terms of its presence or in terms of axis orientation—is also referred to as a scatterer because it scatters the incoming Love wave into a qL wave (Chen and Park, 2013). Henceforth, in this study, we shall use the term "scatterer" to describe an individual gradient detected from qL observations at a single station, while the term "gradient" will refer to a collection of scatterers located in close proximity to each other. Although the polarization of the qL coupled mode is similar to that of Rayleigh wave, its apparent propagation velocity is higher, resulting in its arrival preceding Rayleigh wave. The delay time between the Love and qL arrivals is often small, which suggests that the qL wave travels most of its path as a Love wave (Margheriti et al., 2014).

The criteria for a successful observation of the qL wave can be divided into three main categories: the source, the path, and the near-receiver conditions (Rieger and Park, 2010; Chen and Park, 2013; Margheriti et al., 2014). Naturally, the quality of the seismic record is also important as the qL phase must be distinguishable from the ambient noise. The source criteria pertain to the magnitude and depth of the causative earthquake. The earthquake should be sufficiently large ($Mw \geq 6.5$) to generate significant surface waves, and have a shallow depth to avoid the excitation of surface wave overtones. The path criteria require for the epicentral distance to be larger than 70 degrees for a reasonable separation of Love and Rayleigh waves, and for an anisotropic gradient to be present along the raypath. It is also necessary to demonstrate that the observed polarization anomalies are not related to higher-mode surface waves or other body waves. This can be achieved through a comparison of the observations with full synthetic isotropic seismograms. Finally, the near-receiver criterion necessitates a special geometry between the source, the receiver, and the anisotropic volume. A successful qL observation depends on the angle between the propagation direction and the anisotropic symmetry axis (denoted by ξ). Theoretically, for an anisotropic structure with a horizontal symmetry axis, the intensity of qL observations can be estimated from $\sin(2\xi)$; its absolute value is at a maximum when ξ is either 45° (positively polarized) or 135° (negatively polarized), and is at a minimum when the symmetry axis is either parallel or perpendicular to the propagation direction (Park, 1997; Levin and Park, 1998; Rieger and Park, 2010; Margheriti et al., 2014). In the case of an anisotropy with 45° tilted symmetry axis, the qL intensity may be estimated from $\sin(\xi)$ and is maximized when rays propagate perpendicular to the symmetry axis. Therefore, the presence of a qL wave and its relative amplitude and polarity can be predicted by looking into the FPDs obtained from shear-wave splitting analysis of phases such as the SKS (Rieger and Park, 2010; Chen and Park, 2013; Margheriti et al., 2014). The agreement between the observed and predicted qL polarities serves to confirm that the selected FPDs used for predicting the presence of qL waves accurately represent the anisotropic structure on the receiver side. Fig. 2a illustrates an example depicting the variation in both amplitude and polarization (as represented by $\sin(2\xi)$ values) of the qL phase with a propagation direction of 85° for different FPDs.

To quantify the intensity of the observed qL wave with acceptable signal-to-noise ratio at the stations, two metrics are employed: the energy, obtained by integrating the absolute amplitudes over the desired time window, and the peak-to-peak amplitude ratios of the qL and Love
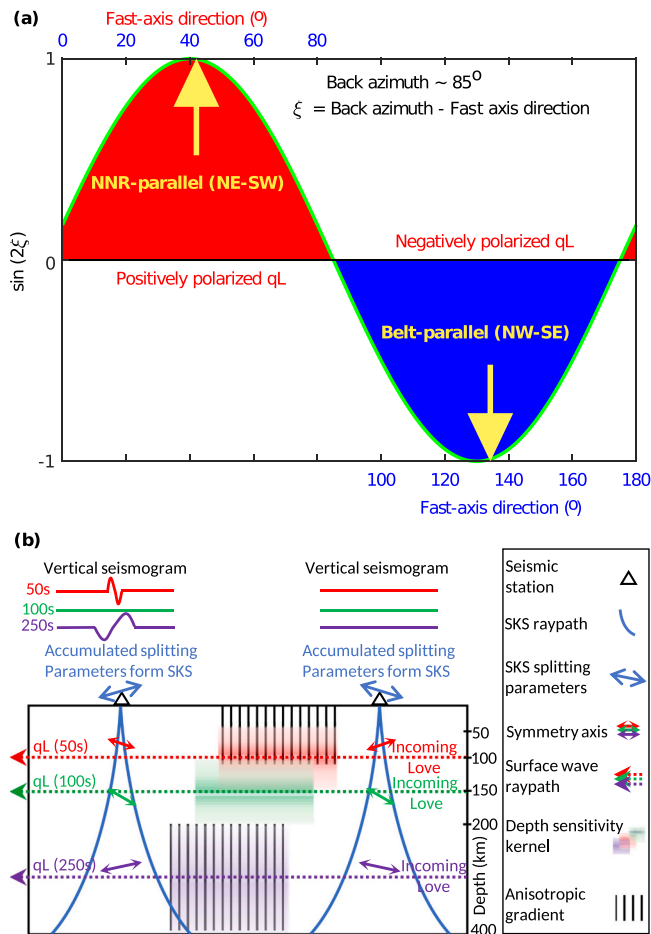
(a)

Fast-axis direction (^{0})

Back azimuth ~ 85^0
ξ = Back azimuth - Fast axis direction

NNR-parallel (NE-SW)

Negatively polarized qL

Positively polarized qL

Belt-parallel (NW-SE)

sin(2ξ)

Fast-axis direction (^{0})

(b)

Vertical seismogram

Vertical seismogram

50s
100s
250s

Accumulated splitting Parameters form SKS

Accumulated splitting Parameters form SKS

Seismic station

SKS raypath

SKS splitting parameters

Symmetry axis

Surface wave raypath

Depth sensitivity kernel

Anisotropic gradient

qL (50s) — Incoming Love
qL (100s) — Incoming Love
Incoming Love
qL (250s) — Incoming Love

Depth (km)

Fig. 2. (a) Variation of sin(2ξ) with fast-axis direction for the average 85° back-azimuth of the Solomon Islands earthquake. The fast-axes causing positive and negative polarization of the qL wave are shown in red and blue respectively. (b) Schematic cartoon illustrating the SKS and quasi-Love (qL) raypaths, along with the approximate depth sensitivity ranges of qL at different periods. Anisotropic symmetry axes and two anisotropic gradients at different depth ranges, and their effect on the vertical seismograms at different periods are also schematically illustrated.

signature along the whole raypath, variation in depth sensitivity of qL with period can offer tangible evidence for the originating depth of the observed anisotropy (Fig. 2b). On the other hand, long-period qL phases exhibit a broad range of depth sensitivity to the structures along the raypath which poses slight difficulties in determining precise depths for the sampled structures. For a horizontal symmetry axis, the qL at 250 s is sensitive to the structures deeper than 200 km. However, as the period decreases, the depth sensitivity range becomes shallower. At 100 s, the depth sensitivity range is around 100–200 km, while at 50 s, it reaches approximately 50–150 km (Park, 1993; Levin and Park, 1998; Chen and Park, 2013). Sensitivity of the qL phase to the lateral variation in anisotropy is also influenced by its frequency content. For the fundamental mode, the angular wavenumber—as a measure of the lateral scale of anisotropic structures that can give rise to qL scattering—is about 1, 11, and 21 at periods of 250, 100 and 50 s, respectively (Park, 1997; Levin and Park, 1998). The angular wavenumbers at periods of 100 and 50 s are approximately equivalent to wavelengths of 3600 and 2000 km, or anisotropic gradients of 900 and 500 km in width, respectively. We varied the cut-off period of the lowpass filtering from 50 s to 100 s in order to investigate the effect of frequency content of the waveforms on the qL observations (Rieger and Park, 2010).

The timing and the shape of the observed qL waveform can provide constraints for the detection and location of abrupt anisotropic gradients along the raypaths (Levin and Park, 1998; Levin et al., 2007; Chen and Park, 2013). To analyze the polarization and timing of the qL observations, we cross-correlated the qL wave on the vertical components and the Love wave on the transverse components, as described by Chen and Park (2013). We determined the polarity of the scattered waves by examining the sign of the cross-correlation coefficients and the time lags between the Love and qL arrivals.

Converting the timing of the qL wave to the distance between receiver and anisotropic gradient is a challenging task. Even slight variations in the difference between the Love and Rayleigh phase velocities can lead to a substantial uncertainty in the converted distance (Chen and Park, 2013). For instance, considering typical Love and Rayleigh phase velocities of 4.5 and 4.0 km/s at 100 s, and assuming a 10 s time lag between Love and qL arrivals, the estimated receiver-scatterer distance is 360 km. However, if the Love phase velocity is increased by only ~2% (0.1 km/s), the distance decreases by about 15% (~55 km). Nevertheless, the technique can constrain the approximate location of the scatterer along the raypath. We used the phase velocities of Love and Rayleigh waves from the GDM52 model of Ekström (2011) to convert the delay times between the Love and qL arrivals to receiver-scatterer distances. We extracted the Love and Rayleigh phase velocities at periods of interest at a locality in central Iran (lat. 33 N and lon. 55E). The relationship $D = (\delta t V_L V_R)/(V_L - V_R)$ was used for the conversion, in which D is the receiver-scatterer distance, δt is the time lag between Love and qL arrivals, and V_L and V_R are the Love and Rayleigh phase velocities, respectively.

3. Results

3.1. Quasi-Love Wave Observations in Western Iran from the 2014 Solomon Islands Earthquake

We used the dataset of the CIGSIP temporary network composed of 63 broadband seismic stations which was deployed for a one-year period in 2013 and 2014 (Fig. 3). Sadeghi-Bagherabadi et al. (2018a,b) examined the core-refracted phases of the earthquakes recorded by the same network to investigate the upper mantle anisotropy through shear-wave splitting analysis. To identify potential polarization anomalies within the Love wave window of the vertical component that could be associated with the qL phase, we performed a visual inspection of waveforms from shallow, large, and well-recorded earthquakes. These earthquakes were selected based on specific criteria outlined in Section 2 of the paper. The aim of this inspection was to identify any deviations
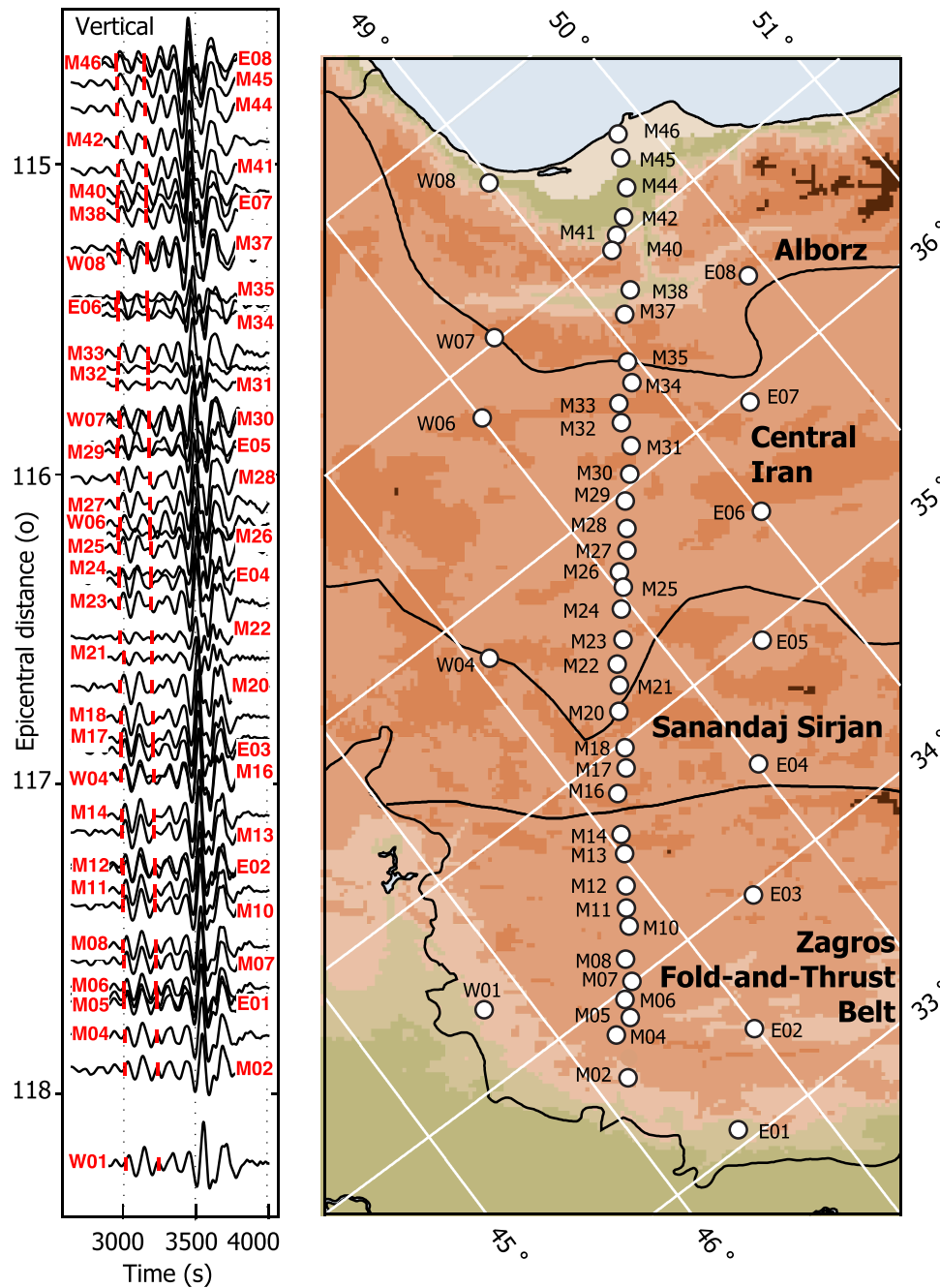
waves (qL/L) (Rieger and Park, 2010; Margheriti et al. 2014). The applied procedure for quantifying the intensity of the qL wave is summarized as follows: (1) We first lowpass filter three-component seismograms with cut-off periods of interest. (2) The horizontal components of the waveforms are then rotated to the great circle path (ZRT coordinate system). (3) A Love wave window is selected between the Love and Rayleigh arrival times which are picked on the transverse and vertical components, respectively. (4) On both horizontal components, the total energy and the largest amplitude in the Love wave window are calculated. (5) On the vertical component, the qL energy and the largest amplitude in the same window (the Love wave window) are calculated. (6) The qL/L ratio as a measure of the amount of scattered Love wave energy with respect to the total recorded Love energy is determined. (7) In a 200-s window prior to the Love wave arrival, the energy of noise on the vertical component and the qL/noise ratio are calculated. If the qL/L ratio (i.e., in the Love window) is greater than the qL/noise ratio, the measurement is retained. Although the results of the energy and peak-to-peak amplitude ratios turned out not to be substantially different, we found that the energy ratio can be affected by the selection of the Love wave window.

The qL phase as a coupled-mode surface wave is, by its nature, depth-sensitive. In contrast to the shear-wave splitting method which does not provide strict depth constraints and accumulates the anisotropic

Fig. 3. Map showing the location of the seismic stations utilized in this study. Vertical components of records of the Solomon Islands earthquake are plotted in the left panel. The qL polarization anomalies are surrounded by red markers.

or irregularities in polarization that could potentially indicate the presence of the qL phase. Based on the quality of the inspected records, we were able to identify clear and distinguishable anomalous waveforms only in the records of the April 12, 2014 Solomon Islands (Mw = 7.6) earthquake (Fig. 3). The vertical components of the records, lowpass filtered at 100 s, are presented in Fig. 3. The polarization anomalies are bracketed by two red markers and their amplitudes are of a considerable percentage of the Rayleigh wave amplitudes.

To verify that the observed polarization anomalies are not associated with higher-mode surface waves or other body waves, we generated a set of synthetic seismograms within the period range of 25–150 s for the full moment tensor of the Solomon Islands earthquake (Nissen-Meyer et al., 2014). The source mechanism was derived from the Global Centroid Moment Tensor (GCMT) solution (Ekström et al., 2012). The

PREM isotropic anelastic velocity model was used to compute 51 synthetics at the recording stations. No body wave or higher mode arrivals were observed within the Love wave time window of the synthetic vertical components, providing additional confirmation that the observed polarization anomalies are indeed associated with the qL waves. An example of the comparison between the observations and the synthetics at station M10 is presented in Fig. 4. The particle motions in the Love wave window (the yellow area in Fig. 4b) are also illustrated. The vertical and transverse components of the individual stations are presented in Fig. 5. To facilitate comparison, the synthetic seismograms computed at five stations are also plotted in the top row.
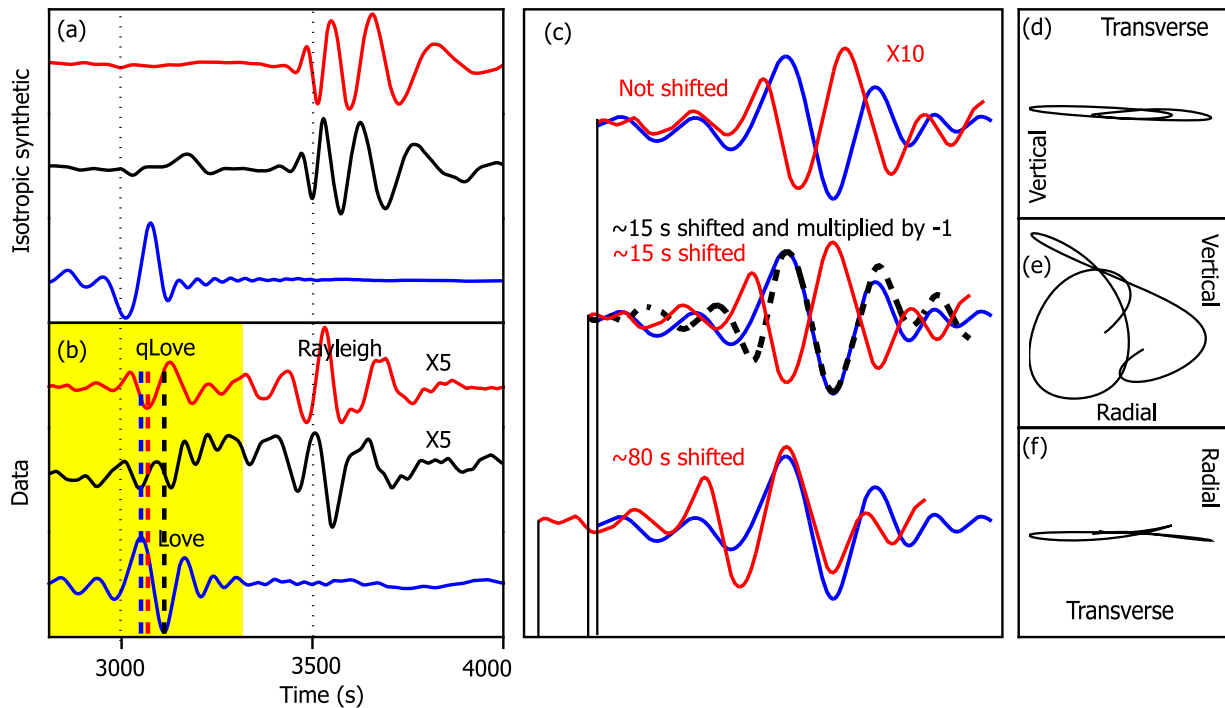
Fig. 4. Comparison of the isotropic synthetic seismograms calculated at station M10 with the observed records at the same station. (a) Three component synthetic seismograms lowpass filtered at 100 s. Vertical, radial and transverse components are shown in red, black and blue, respectively. The vertical and radial components are scaled proportionally to the maximum amplitude of the transverse component. The synthetic seismograms were manually adjusted by slightly shifting them to approximately align the synthetic Love wave packet with the observed Love wave packet in (b). (b) Three component records of station M10. The blue dashed line represents the highest peak of the Love wave. The red and black dashed lines represent the lowest trough of the qL and Love waves, respectively. The yellow area is the Love wave time window enlarged in panel c. (c) Transverse (blue) and scaled vertical (red) components of the time window shown in (b). At the top, the components are plotted without time shifting. In the middle, the vertical component is reversed and shifted by about -15 s. This is the time lag derived from the maximum absolute correlation coefficients assuming that the qL wave is negatively polarized. In the bottom, it was assumed that the qL polarization is positive, which required a time shift of -80 s to match the two components. (d), (e), and (f) Particle motions in the Love wave window of the M10 record.

3.2. Quantifying the Intensity of the Observed Quasi-Love Waves

The qL/L ratio for the records of all stations lowpass filtered at 100 s are indicated in Fig. 5. The ratio values vary from 4.5% to 8.4%, with higher values in the CIGSIP stations in the Zagros (hereafter Zagros stations), gradually decreasing toward the CIGSIP stations in central Iran (hereafter central Iran stations) and again slightly increasing in the CIGSIP stations in the Alborz (hereafter Alborz stations). All the detected quasi-Love phases, even those with lowest qL/L ratios have acceptable signal-to-noise ratios and distinguishable amplitudes in comparison to the pre-arrival noise window. Since we have been able to observe a range of qL amplitudes throughout our study region, rather than just reporting the presence or absence of qL, we can discuss the relative strength of qL development in different parts of the study region in terms of quantitative parameters.

3.3. Period Dependence, Polarization and Timing of Quasi-Love Observations

The vertical and transverse components of the records, lowpass filtered at different periods, are presented in Figs. S1–S5 and their qL/L ratios are listed in Table S1. The projected ratios along the main profile of the seismic array and their smoothed trends are illustrated in Fig. 6b. The darker colors represent longer cut-off periods and lighter colors are for shorter cut-off periods. Overall, the short-period cut-off filters result in higher qL/L ratios, but while this period-dependence is negligible at the Zagros and central Iran stations, at the Alborz stations, significant variation is observed in the qL/L ratio between the filters.

A comparison of the timing of peaks and troughs of the qL and Love waves in Fig. 5 hints that the qL waves at most of the stations in the

Zagros and central Iran are negatively polarized, whereas at the Alborz stations, they are positively polarized. These agree with the calculated negative correlation coefficients in the Zagros and central Iran, and positive coefficients in the Alborz. Fig. 4 shows an example of opposite polarization of the qL and Love waves at station M10 in the Zagros. We also considered the possibility of positive polarization at the Zagros and central Iran stations (e.g., Fig. 4c) and estimated the time lags required to produce such polarization. The estimated time lags of 80–100 s obtained from the largest positive correlation coefficients suggest that the scatterers should be at a distance of more than 30 degrees from the stations. It would, however, be highly unlikely for such a distant gradient to produce the observed large qL/L ratios in the Zagros. In fact, it turned out that the absolute values of the correlation coefficients calculated assuming positive polarization are much smaller than those calculated based on the assumption of negative polarization. We applied the same procedure to waveforms filtered at different cut-offs in order to determine their polarity and timing. Although the polarities of the observations are not affected by filtering, we found that the time lags at the stations in the interior of the Zagros can be influenced by the cut-off period of the filters (Fig. 6c).

3.4. Comparison of Quasi-Love Observations and Splitting Measurements

The Solomon Islands earthquake fulfilled all the source and path criteria for observation of qL in Iran, i.e., a large magnitude of Mw 7.6, a shallow depth of ~20 km, and a large epicentral distance of 116° (Fig. S6). For our event-station raypaths, potential distant anisotropic gradient regions, such as those across the major plate boundaries in the South China Block and Tibet (Bird, 2003), may cause qL scattering (Fig. S6). The scattering generated from such distant gradient regions,
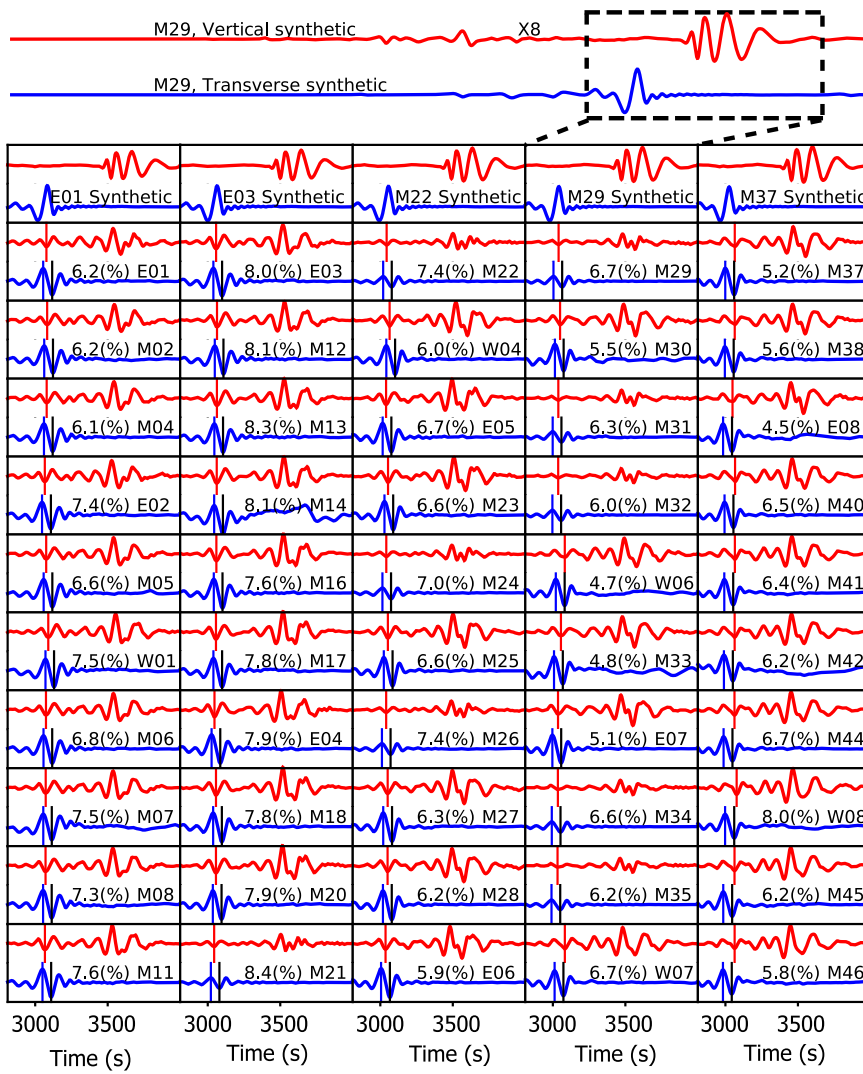
Fig. 5. Vertical (red) and Transverse (blue) components of records of the Solomon Islands earthquake lowpass filtered at 100 s. The vertical components are scaled by a factor of 8 and the observed qL/L percentage at each station is mentioned. Isotropic synthetic records calculated at E01, E03, M22, M29 and M37 stations are presented (top row) to facilitate the comparison. The synthetic seismograms were manually adjusted by slightly shifting them to approximately align the synthetic Love wave packet with the observed Love wave packets. The blue bars represent the highest peaks of the Love wave. The red and black bars represent the lowest trough of the qL and Love waves, respectively. In the Zagros and central Iran stations (shown in the left and middle columns), the Love peak (blue bars) precede the qL trough (red bars), and the Love trough (black bars) arrives after the qL trough, implying opposite polarity of the qL and Love waves. In contrast, at the Alborz stations in the northern part of the network (last column on the right), the Love trough precedes the qL trough, indicating that the qL waves are positively polarized.
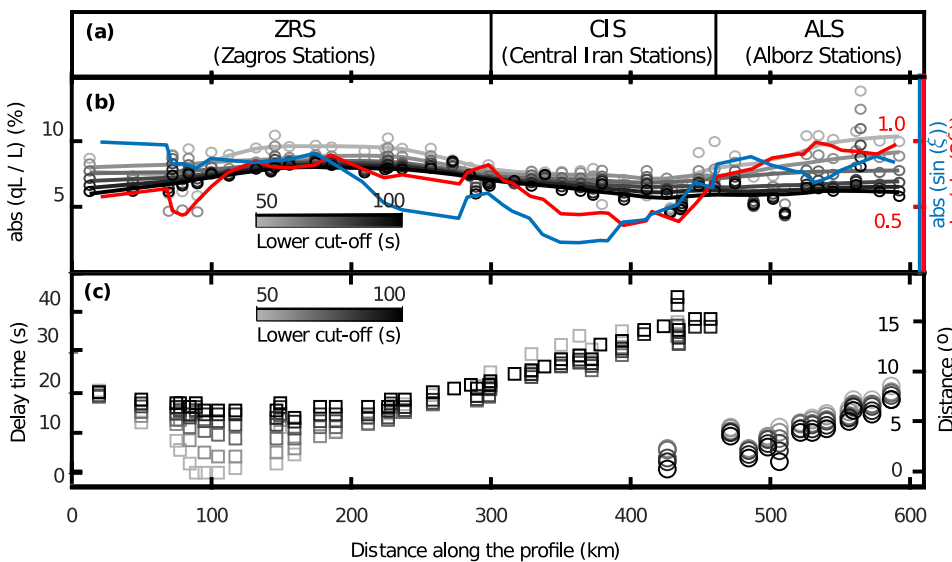

Fig. 6. Variations in qL/L ratio and delay time between Love and qL along the main seismic profile. (a) Borders of the principal tectonic provinces along the profile. (b) The qL/L ratios with different cut-off periods (50–100 s) shown by circles. The undulating lines are the smoothed trends of the markers with the same colors. Red and blue lines are the smoothed trend of $\sin(2\xi)$ and $\sin(\xi)$, respectively. (c) The delay times between Love and qL arrivals and the corresponding receiver-scatterer distances for different periods. Delay times and distances for stations with opposite polarity of Love and qL are shown by squares and those with positively polarized qL are shown by circles.

however, is expected to uniformly increase the level of qL energy at all of the stations since all of the rays pass through those regions. This is in contrast with the observed variation in the qL/L ratios along the profile (Fig. 6). Conversely, a near-distance anisotropic gradient will result in abrupt variations in the qL observations along the network, as only those stations with event-station rays sampling the gradient region will exhibit qL energy on their recordings. Therefore, the presence of near-receiver anisotropic gradients combined with a suitable geometry between the raypaths and the anisotropic axis determines whether a successful qL observation along the seismic network is possible.

To understand how the SKS-derived anisotropic pattern relates to the qL anisotropic evidence, we compared the qL/L ratios lowpass filtered at different periods with the sin(ξ) and sin(2ξ) values calculated using the SKS-derived fast axes from the seismic profile used in this study (Sadeghi-Bagherabadi et al., 2018a). Fig. 6b displays the qL/L ratios at individual stations and the trend of absolute sin(ξ) and sin(2ξ) variations projected along the main seismic profile. Both the sin(ξ) and sin(2ξ) functions have high values at the stations in the interior of the Zagros

region and sin(2ξ) approaches its maximum value of 1 at the Alborz stations, indicating that in those parts of the network, the raypaths make a proper angle with the anisotropic axis to excite high-amplitude qL waves. At the central Iran stations, the sin(2ξ) value is around 0.5, which means the raypaths arrive either sub-parallel or sub-perpendicular to the local anisotropic axis. The pattern of sin(2ξ) variation across the network is in rough agreement with the variation in qL/L ratio. This indicates that the development of high-amplitude qL waves at the Zagros stations and high-amplitude short-period filtered waves at the Alborz stations, might partly be due to the existence of suitable near-receiver conditions in those regions. Additionally, the positive sin(2ξ) values at the Alborz stations and the negative sin(2ξ) values at the Zagros and central Iran stations (Fig. 2a) are consistent with the observed qL polarities at the corresponding stations (Figs. 5 and 6c). This alignment further supports the notion that near-receiver anisotropy, as indicated by shear-wave splitting analysis, may account for the variation of qL/L ratios along the profile.
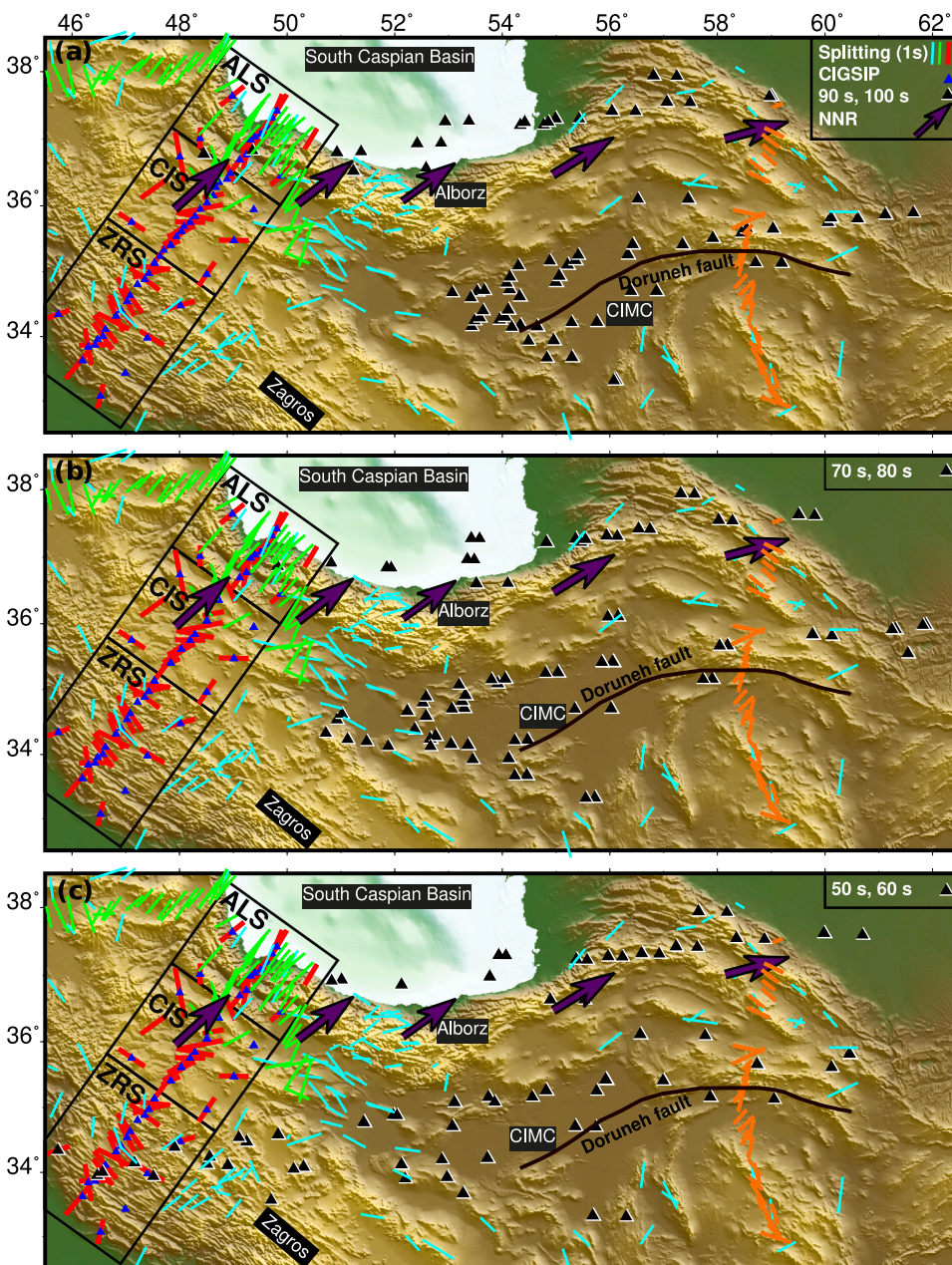

Fig. 7. Back-projected locations of the anisotropic scatterers estimated using the time lag between Love and qL arrivals, and the Love and Rayleigh phase velocities (black triangles) obtained from the lowpass filtered waveforms with cutoff periods 100 s and 90 s (a), 80 s and 70 s (b), and 60 s and 50 s (c). Blue triangles are the recording stations. The splitting results of Sadeghi-Bagherabadi et al. (2018a), Arvin et al. (2021), Kaviani et al. (2021) and Gao et al. (2022) are presented by red, green, cyan and orange bars, respectively. The absolute plate motion velocity vectors in the no-net-rotation (NNR) reference frame are illustrated by arrows.

3.5. Estimation of the Approximate Locations of the Anisotropic Gradients

Fig. 6c shows the receiver-scatterer distances for different filter cut-offs projected along the main array line. The delay times and distances of waveforms with opposite-polarity qL and Love waves are marked by squares, and those with positive polarity by circles. Fig. 7 and S7 show the back-projected locations of the scatterers from different periods for stations with significant qL observations. The scatterer locations for the Zagros stations vary significantly with the filter cut-off period, whereas those for the Alborz stations are less affected.

Based on the back-projections shown in Fig. 7, we identified three possible principal anisotropic gradient regions as sketched in Fig. 8. The location of the first gradient is estimated by back-projection of the receiver-scatterer distances at the Zagros stations (Fig. 7). The eastern part of this gradient extends along the boundary between central Zagros and central Iran (GE1) and rotates counterclockwise towards its western end, where it penetrates the western Zagros (GW1). The cut-off period related to these scatterers decreases from the eastern part of the gradient (GE1) to the western part (GW1). Such period-dependent locations of the scatterers may arise from various factors, including the depth, lateral extent, and shape of the anisotropic gradient. However, if we assume the depth of the gradient as a straightforward and plausible explanation for the period dependence, it can offer valuable insight into the depth of the underlying anisotropic structures. It is intriguing that the period-dependent location of the scatterers in this gradient mimics the trend of FPDs in the same region (Figs. 7 and 8). The second gradient region (G2) is composed of the scatterers back-projected from the central Iran stations (Fig. 7) where the lowest qL/L ratios and sin(2ξ) values are obtained (Fig. 6). The G2 gradient is located along the boundary between the CIMC to the south and Kopet Dagh Mountains to the north for all period ranges (Fig. 8). The third gradient (G3) is extended along the Kopet Dagh Mountains and the southern coastline of the Caspian (Fig. 8). The location of the scatterers in G3 stays relatively stable with different cut-off periods, but the corresponding qL/L ratios observed at the Alborz stations are much higher at shorter periods (Fig. 6b).

4. Discussion

4.1. Lateral Variation in the Downward Dip of the Arabian Lithosphere Along Central Zagros Inferred from the Depth-dependent Anisotropic Scatterers

The SKS splitting results at the CIGSIP stations in the northwesternmost part of the Zagros exhibit NW-SE directed fast-axes sub-parallel to the strike of the range (Fig. 7) (Sadeghi-Bagherabadi et al., 2018a,b). The NW-SE trend of the splitting measurements is also observed in the adjacent central Iran by Kaviani et al. (2021) (Fig. 7). The negative values of sin(2ξ) in this region obtained from the NW-SE trend of FPDs predict that the polarity of the qL wave should be flipped relative to the Love wave (Fig. 2a). This is in accord with the observed negatively polarized qL waves at the Zagros stations and implies that the qL wave is developed as a result of a nearby anisotropic gradient to the east of the NW-SE FPDs. Such an abrupt FPD change is observed in the boundary zone of the Zagros and central Iran which coincides fairly well with the estimated position of the anisotropic gradient marked as GE1 in Fig. 8. The easternmost scatterers in the GE1 gradient are obtained from the waveforms filtered at longer periods (cut-off at 90–100 s) and thus pertain to scatterers in deeper structures. The scatterers tend to have shorter period content (cut-off at 60–70 s) and get shallower from east to west of the gradient. The GE1 gradient follows a NW-SE trend parallel to the Zagros strike and coincides with the observed belt-parallel trend of the FPDs along the southwestern margin of the CIMC and northeastern margin of the Zagros. These NW-SE splitting measurements have been interpreted to represent an asthenospheric flow caused by a thick Zagros lithospheric root (Priestley et al., 2012) and circular flow around the Zagros keel (Kaviani et al., 2021). To the east of these scatterers in the interior of central Iran the FPDs rotate to a prominently N-S direction (Kaviani et al., 2021; Gao et al., 2022) indicating that the GE1 is located in the region where the direction of anisotropy changes from a N-S trend in the eastern central Iran to NW-SE at the boundary between the Zagros and central Iran (Fig. 8).

While the earlier tomography results by Hafkenscheid et al., (2006) and Priestley et al. (2012) did not have sufficient resolution to image the fine features along the Zagros belts, recent higher-resolution tomographic imaging studies revealed a lateral variation in the depth and the downward dip of the Arabian continental lithosphere beneath the CIMC (e.g., Veisi et al., 2021; Mohammadi et al. 2022). In the central Zagros, their results demonstrate that the downward dip of the Arabian
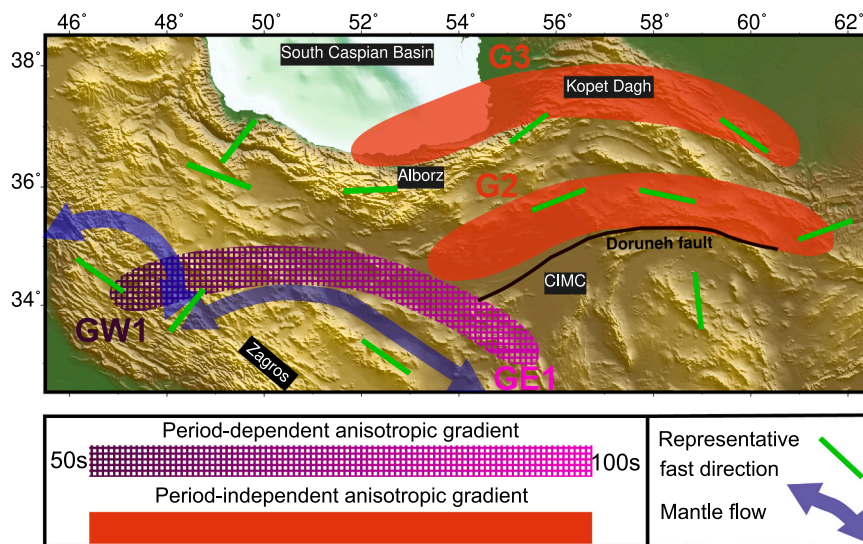

Fig. 8. The simplified sketches showing the approximate locations of the GE1, GW1, G2 and G3 anisotropic gradients. Representative fast directions are shown by green bars. The proposed mantle flow caused by the thick Zagros lithosphere and the lithospheric discontinuity in the western Zagros is also depicted.
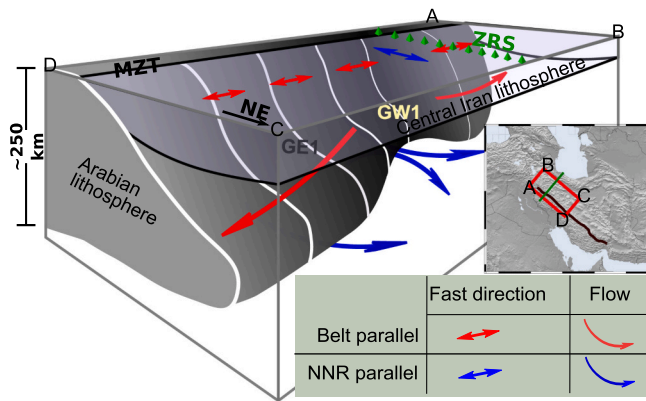
Fig. 9. (a) A simplified sketch illustrating the state of the lithosphere as well as the representative observed fast polarization directions and proposed mantle flow beneath the central and western Zagros (the red box area in the inset map). Abbreviations are defined as follows: MZT, Main Zagros thrust; ZRS, Zagros stations of the seismic array.

lithosphere beneath central Iran is steeper to the east and shallower to the west (Fig. 9). The period/depth dependence of the scatterers along the GE1 gradient is in agreement with the reported variation in the geometry of the Arabian lithosphere. The steeper dip of the Arabian lithosphere to the east leads to a deeper asthenospheric flow which in turn results in a deeper anisotropic gradient (~120–240 km) between the dominant N-S FPDs in eastern central Iran and the NW-SE FPDs at the Zagros-central Iran boundary. Similarly, the shallower dip of the Arabian lithosphere towards west leads to a shallower anisotropic gradient (~100–180 km) in the western part of GE1 (Figs. 8 and 9).

4.2. Anisotropic Gradient Beneath the Western Zagros as an Evidence for Lateral Lithospheric Discontinuity Along the Zagros Strike

Different geodynamical hypotheses have been proposed for the western Zagros which should exhibit clear anisotropic signatures of their own. Priestley et al. (2012) and Kaviani et al. (2021) argued that the NW-SE FPDs in central Iran originate from an asthenospheric flow around the root of the Zagros. Sadeghi-Bagherabadi et al. (2018b) proposed two geodynamic scenarios based on the lithospheric structure in the western Zagros and elucidated the link between the scenarios and the dense splitting measurements. They considered the possibility of both asthenospheric and lithospheric origins of the NW-SE FPDs in the westernmost part of the Zagros and concluded that the fast directions might have their origins in the ~200-km-thick lithosphere beneath the Zagros.

The receiver-scatterer distances from the Zagros stations at longer periods point to the positions at the boundary between the Zagros and central Iran, whereas the locations of some of the scatterers obtained from the shorter cut-off periods (i.e., 50 s, 60 s and 70 s) gradually migrate westward to a location very close to the Zagros stations (Figs. 7 and S7). This implies that the shorter period qL scattering in the western Zagros is due to the presence of a shallower anisotropic gradient (GW1) at a very short distance to the east of the Zagros stations (Fig. 8). While the FPDs at the Zagros stations obtained by Sadeghi-Bagherabadi et al. (2018a) are parallel to the Zagros strike (NW-SE), Kaviani et al. (2021) obtained NE-SW fast directions not so far from the Zagros stations of the CIGSIP. Their FPDs are sub-parallel to the APM vectors in the no-net-rotation (NNR) reference frame (Figs. 7 and 8). The location of the GW1 gradient is in accord with the abrupt variation of the FPDs from the belt-parallel trend at the Zagros stations to the NNR-parallel observations to the east of the Zagros stations (Figs. 7 and 8). The location of the gradient also corresponds to the boundary between the recently observed low-velocity zone in the ~150–400 km depth range to the east (Mahmoodabadi et al., 2020; Movaghari and Doloei, 2020; Movaghari

et al., 2021; Veisi et al., 2021; Irandoust et al., 2022) and the high-velocity structure reported by Rahmani et al. (2019) and Veisi et al. (2021) to the west (Figs. 8 and 9). The western higher-velocity structure beneath the Zagros stations has been interpreted to represent the depth continuation of the continental lithosphere which might still be partially connected to the subducted oceanic slab at more than 400 km depth (Veisi et al., 2021). According to the tomographic imaging of Veisi et al. (2021), the thickness of the lithosphere beneath the western Zagros dramatically decreases from ~300 km to ~150 km to the east of the Zagros stations and increases again to ~300 km further to the east. This lateral discontinuity in the Zagros lithosphere coincides with the NNR-parallel splitting measurements reported by Kaviani et al. (2021).

Fig. 9 schematically illustrates the current state of the lithosphere beneath the western Zagros compiled from Rahmani et al. (2019), Mahmoodabadi et al. (2020), Veisi et al. (2021), Irandoust et al. (2022) and Mohammadi et al. (2022). It suggests that the structure of the Zagros lithosphere significantly changes across the GW1 gradient in terms of the seismic velocity structure and the mantle flow field within the depth range of 100–200 km. Taking these differences into account, one may argue that the NW-SE FPDs in this depth range beneath the Zagros stations are mainly caused either by an asthenospheric toroidal flow around the local thick lithosphere (Kaviani et al., 2021), or by lithospheric deformation (Sadeghi-Bagherabadi et al., 2018a,b). However, slightly to the east, the larger-scale NE-directed asthenospheric flow through the lithospheric gap can act as the principal contributor to the NNR-subparallel SKS fast directions. Therefore, the GW1 gradient can be considered as a clear anisotropic signature of the lithospheric lateral discontinuity and the associated geodynamic processes in the western Zagros.

4.3. Doruneh Fault as a Lithospheric-scale Boundary

A significant concentration of scatterer locations for all cut-off periods is clustered along the northern margins of the CIMC (marked as G2 in Fig. 8). These locations were estimated by back-projecting the receiver-scatterer distances at the central Iran stations. The receiver-scatterer distances as shown in Fig. 6 reach a maximum at the central Iran stations, and their period dependence and the qL/L values are small (Fig. 6). Splitting measurements by Kaviani et al. (2021) and Gao et al. (2022) exhibit a complex pattern of the FPDs along the G2 gradient (Figs. 7 and 8). While the qL wave can arise from such a variable pattern of the fast-axis directions, making inferences on the intensity of the observed qL waves from the sin(2ξ) values may not be straightforward as elaborated on in the following. The fast-axis directions at the central Iran stations are subparallel to the qL propagation direction (i.e., E-W) as denoted by the minimum values of sin(2ξ). The small sin(2ξ) values at the central Iran stations suggests that the very near-receiver anisotropic condition (i.e., the local E-W trending FPDs observed at the stations) may cause the small qL/L values. However, the large receiver-scatterer distances obtained at the same stations (Fig. 6) and the reported more distant variable FPDs along the raypaths to east (Figs. 7 and 8) contradict the idea of a very near-receiver gradient. Moreover, the measured qL/L ratios at these stations are not as small as the low values predicted from sin(2ξ). Therefore, a more realistic scenario is that the observed qL waves at the central Iran stations can be generated as a result of the complex pattern of FPDs in the north of the Doruneh fault and the south of the Kopet Dagh Mountains (Fig. 8) rather than an anisotropic gradient very close to the central Iran stations. This explanation is in agreement with the calculated large receiver-scatterer distances (Fig. 6c). Considering the different quality factors of the Love and Rayleigh wave propagations, a 900-km increase in the travel paths of the qL and Love waves accounts for a 1% decrease in the qL/L amplitude ratio (Rieger and Park, 2010). From the results in Fig. 6, it turns out that the receiver-scatterer distances for the central Iran stations (~2000 km) are about twice as large as those of the Zagros stations (~1000 km) and the minimum qL/L ratios recorded at the central Iran stations is about 2% smaller than the

maximum qL/L at the Zagros stations. As a result, we can conclude that the scattered waves arriving at the central Iran stations travel larger distances and therefore are more attenuated than those arriving at the Zagros stations. This can explain the relatively weaker presence of the qL wave in the middle part of the CIGSIP array.

Recent imaging studies have revealed complex lithospheric and sub-lithospheric structures beneath the CIMC. Motaghi et al. (2015) and Wei et al. (2019) reported a low-velocity structure deeper than ~100 km beneath the CIMC. Wei et al. (2019) imaged an inverted cone-shaped low-velocity body in the upper mantle beneath CIMC. The western part of the G2 gradient is found to trace the boundary of the low-velocity zone at depth based on comparison of the tomographic images and the locations of the scatterers. The spatial coincidence between the western scatterers in the G2 gradient and the lateral variation in the deep velocity structure suggests that the longer-period scatterers may have originated from the lateral variation in the sub-lithospheric flow field at the western margin of CIMC.

According to Wu et al. (2021), a notable feature in the region is the increase in both crustal and lithospheric thickness across the Doruneh fault. The S receiver function study by Wu et al. (2021) revealed that the lithosphere of the CIMC (~90 km) is thinner than the lithosphere of the Kopet Dagh (~120 km). They reasoned that the difference in the lithospheric thickness could be due to convective flow in the sub-lithospheric volatile-enriched and melt-metasomatized low-velocity layer beneath the CIMC. The shear-wave splitting results of Gao et al. (2022) also exhibit abrupt variations in the FPDs and in their source layer across the G2 gradient. They interpreted the NNE-SSW trending FPDs to the south of the Doruneh fault to originate from the asthenospheric flow beneath a weakly anisotropic lithosphere, whereas to the north of the Doruneh fault the belt-parallel (NW-SE) FPDs represent lithospheric deformation. Such an abrupt variation in the lithospheric thickness and FPDs across the Doruneh fault indicates different styles of lithospheric deformation to its north and south. In contrast to the lithosphere in the south, the lithosphere to the north has undergone substantial thickening and shortening. It also signifies the role of the Doruneh fault as a major shear zone and lithospheric boundary that separates geological domains with different deformation histories. The FPDs estimated by Kaviani et al. (2021) along the G2 gradient rotate gradually from NW-SE to the east to NE-SW to the west, following a trend similar to the curvature in the strike of the Kopet Dagh. In conclusion, the shorter period scatterers in the G2 anisotropic gradient arise from the deformation in the thickened lithosphere to the north of the Doruneh fault.

4.4. Anisotropic Scatterers in the Kopet Dagh Originating from Vertically-coherent Lithospheric Deformation

The thickness of the lithosphere decreases from more than 200 km beneath the Zagros to around 100 km in the Alborz. The qL observations' frequency dependence reaches a peak at the Alborz stations (Fig. 6b). Taking into account that northern central Iran and Alborz have a thin lithosphere, the longer-period qL waves observed at the Alborz stations are more sensitive to the asthenosphere, whereas the shorter-periods mainly sample the lithosphere. The large sin(2ξ) values predict a favorable near-receiver condition for the successful observation of the prominent qL wave at the Alborz stations (Fig. 6b). The predicted prominent presence of the qL wave is consistent with qL observations at shorter periods. For the longer cut-off periods, the values of the qL/L ratios are considerably smaller, implying that the anisotropic gradient generating the qL wave should be in shallower structures.

The receiver-scatterer distances estimated from the stations at the southern edge of Alborz are less than 5 degrees, almost the same range as those estimated from the Zagros stations (Fig. 6c). This implies that the anisotropic gradient generating the qL waves observed at the stations in the southern edge of the Alborz should be close to the stations and in the boundary zone between the eastern Alborz and the South Caspian Basin (SCB) (Fig. 7). This anisotropic gradient is represented by the

westernmost end of G3 in Fig. 8. The western part of the G3 gradient is aligned with the border between the maximum clockwise and counter-clockwise rotation rates in the Alborz and SCB, respectively (Khorrami et al., 2019), suggesting that deformation styles in these regions are not similar. Furthermore, different geophysical studies have shown that the lithosphere beneath the SCB is notably thicker (~220 km) than the lithosphere beneath the western Alborz (~100 km) (Motavalli-Anbaran et al., 2011; Jimenez-Munt et al., 2012; Rastgoo et al. 2018). Therefore, one can conclude that contrast in lithospheric thickness, as well as variation in the style of deformation may contribute to the western part of the G3 gradient along the border between eastern Alborz and the SCB.

Toward the northern end of the seismic profile, the receiver-scatterer distances slightly increase (Fig. 6c) and the scatterer locations migrate from the boundary between the eastern Alborz and SCB to the Kopet Dagh Mountains (Fig. 7). The approximate location of this group of scatterers is represented by the central and eastern parts of the G3 gradient in Fig. 8. The geodetic velocity field in the NNR reference frame is believed to act as a proxy for the fast-axis orientation of the sub-lithospheric material. The NNR velocity vectors in the Alborz and Kopet Dagh do not exhibit any abrupt variations and an anisotropic gradient in the asthenosphere of that region is thus unlikely (Fig. 7). On the other hand, Sadeghi-Bagherabadi et al. (2018b) argued that the oroclinal bending process could influence the pattern of lithospheric deformation and fast-axis orientations along the mountain belts. Therefore, considering the bend in the trend of the Kopet Dagh Mountains, variation in the pattern of lithospheric anisotropy along the range is expected. The reported variation in the splitting measurements between the eastern and western parts of the Kopet Dagh provides evidence for the existence of such lithospheric anisotropic gradient (Kaviani et al., 2021; Gao et al., 2022).

The eastern and central part of the G3 gradient is spatially correlated with the areas of higher strain-rate along the Kopet Dagh Mountains (Khorrami et al., 2019) where the lithosphere is known to be shortened and thickened (Wu et al., 2021). The shortest period of qL observations at 50 s with a depth sensitivity range of ~50–150 km barely samples the crustal part of the lithosphere, hinting that the qL is mainly generated by the scatterers in the lithospheric mantle in this region. The agreement between the surface crustal deformation inferred from the strain map and locations of the scatterers in the lithospheric mantle provides a key piece of support for the coupling of the crustal and lithospheric mantle, and the vertically-coherent deformation of the lithosphere of the Kopet Dagh Mountains.

5. Conclusions

We used 51 seismic records of the Solomon Islands earthquake recorded by the CIGSIP temporary network in the western Arabia-Eurasia collision zone in order to investigate the presence of qL waves. We quantified the intensity of the qL wave observations by calculating the peak-to-peak amplitude ratios of the qL and Love waves at different period ranges. We also determined the qL timing and polarity. The intensities of qL wave exhibit a variation from period-independent and high-amplitude observations in the Zagros stations to weaker observations in central Iran stations and more prominent shorter period qL waves toward the CIGSIP stations in Alborz. The Zagros and central Iran stations recorded negatively polarized qL waves, while qL waves at the Alborz stations were positively polarized. The opposite polarity of the qL and Love waves conform to the dominant NW-SE fast-axis orientations reported by shear-wave splitting studies in the western Zagros and central Iran stations. The similarity between the qL and the Love wave polarizations in the Alborz stations is also compatible with the NE-SW trend of the fast-axes in the same stations. The time lags between Love and qL arrivals are highly influenced by the frequency content of the waveforms recorded at the Zagros stations. In contrast, the qL timing is not period-dependent in the CIGSIP stations of central Iran and Alborz. We used the timing of qL waves to map the back-projected locations of

the scatterers. The short-period scatterers related to the Zagros stations are very close to the stations, whereas the longer-period qL scatterings at the same stations are caused by a farther anisotropic gradient positioned along the southwestern margin of the central Iran micro-continent. Taking these results and recent tomographic images into account, the following principal conclusions can be drawn:

- The shorter-period (50 −70 s) qL waves recorded in the western part of Zagros are formed as a result of an anisotropic gradient caused by lateral lithospheric discontinuity along the Zagros strike. The NW-SE trend of fast-axis directions to the west of the gradient originates from either the toroidal flow around the locally thick lithosphere or lithospheric deformation, whereas the belt-perpendicular fast-axis directions to the east of the gradient are caused by the large-scale asthenospheric flow through the lithospheric gap.
- The scatterers' locations along the Zagros and central Iran boundary zone tend to exhibit a decrease in period from east to west, suggesting that the anisotropic gradients are deeper to the east and shallower to the west. This agrees with the recently observed variation in the downward dip of the Arabian lithosphere beneath central Iran which is steeper to the east and shallower to the west.
- In eastern Iran, the anisotropic gradient to the north of the Doruneh fault and south of the Kopet Dagh Mountains corresponds to the reported variations in lithospheric thickness and sub-lithospheric velocity anomalies across the Doruneh fault. This indicates that the Doruneh fault represents a major shear zone and lithospheric boundary separating the geological domains with different histories of deformation.
- The spatial distribution of the anisotropic gradients correlates with the areas with higher surface strain-rates along the Kopet Dagh Mountains, suggesting a possibility of vertically-coherent style of lithospheric deformation along the mountain range.

CRediT authorship contribution statement

Margheriti Lucia: Conceptualization, Data curation, Formal analysis, Funding acquisition, Investigation, Methodology, Project administration, Resources, Software, Supervision, Validation, Visualization, Writing – original draft, Writing – review & editing. **Aoudia Abdelkrim:** Conceptualization, Data curation, Formal analysis, Funding acquisition, Investigation, Methodology, Project administration, Resources, Software, Supervision, Validation, Visualization, Writing – original draft, Writing – review & editing. **Sadeghi-Bagherabadi Amir:** Conceptualization, Data curation, Formal analysis, Funding acquisition, Methodology, Project administration, Investigation, Resources, Software, Supervision, Validation, Visualization, Writing – original draft, Writing – review & editing. **Sobouti Farhad:** Conceptualization, Data curation, Formal analysis, Funding acquisition, Investigation, Methodology, Project administration, Resources, Software, Supervision, Validation, Visualization, Writing – original draft, Writing – review & editing. **Baccheschi Paola:** Conceptualization, Data curation, Formal analysis, Funding acquisition, Investigation, Methodology, Project administration, Resources, Software, Supervision, Validation, Visualization, Writing – original draft, Writing – review & editing. **Lucente Francesco Pio:** Conceptualization, Data curation, Formal analysis, Funding acquisition, Investigation, Methodology, Project administration, Resources, Software, Supervision, Validation, Visualization, Writing – original draft, Writing – review & editing.

Declaration of Competing Interest

The authors declare that they have no known competing financial interests or personal relationships that could have appeared to influence the work reported in this paper.

Data Availability

The qL/L ratios for different cut-off periods (50 s to 100 s) are available in Table S1 of the supplementary material. The raw waveforms used in this study are available at https://doi.org/10.5281/zenodo.8256578.

Appendix A. Supporting information

Supplementary data associated with this article can be found in the online version at doi:10.1016/j.jog.2023.101989.

References

Arvin, S., Sobouti, F., Priestley, K., Ghods, A., Motaghi, K., Tilmann, F., Eken, T., 2021. Seismic anisotropy and mantle deformation in NW Iran inferred from splitting measurements of SK (K) S and direct S phases. Geophys. J. Int. 226 (2), 1417–1431. https://doi.org/10.1093/gji/ggab181.

Bird, P., 2003. An updated digital model of plate boundaries. Geochem., Geophys., Geosystems 4 (3). https://doi.org/10.1029/2001GC000252.

Chen, X., Park, J., 2013. Anisotropy gradients from QL surface waves: evidence for vertically coherent deformation in the Tibet region. Tectonophysics 608, 346–355. https://doi.org/10.1016/j.tecto.2013.09.019.

Dashti, F., Lucente, F.P., Motaghi, K., Bianchi, I., Najafi, M., Govoni, A., Shabanian, E., 2020. Crustal scale imaging of the Arabia-Central Iran collision boundary across the Zagros suture zone, west of Iran. Geophys. Res. Lett. 47 (8), e2019GL085921 https://doi.org/10.1029/2019GL085921.

Ekström, G., 2011. A global model of Love and Rayleigh surface wave dispersion and anisotropy, 25–250 s. Geophys. J. Int. 187 (3), 1668–1686. https://doi.org/10.1111/j.1365-246X.2011.05225.x.

Ekström, G., Nettles, M., Dziewoński, A.M., 2012. The global CMT project 2004–2010: centroid-moment tensors for 13,017 earthquakes. Phys. Earth Planet. Inter. 200, 1–9. https://doi.org/10.1016/j.pepi.2012.04.002.

Gao, Y., Chen, L., Talebian, M., Wu, Z., Wang, X., Lan, H., Zhu, R., 2022. Nature and structural heterogeneities of the lithosphere control the continental deformation in the northeastern and eastern Iranian plateau as revealed by shear-wave splitting observations. Earth Planet. Sci. Lett. 578, 117284 https://doi.org/10.1016/j.epsl.2021.117284.

Hafkenscheid, E., Wortel, M.J.R., Spakman, W., 2006. Subduction history of the Tethyan region derived from seismic tomography and tectonic reconstructions. J. Geophys. Res.: Solid Earth 111 (B8). https://doi.org/10.1029/2005JB003791.

Irandoust, M.A., Priestley, K., Sobouti, F., 2022. High-Resolution Lithospheric Structure of the Zagros Collision Zone and Iranian Plateau. J. Geophys. Res.: Solid Earth 127 (11), e2022JB025009. https://doi.org/10.1029/2022JB025009.

Jimenez-Munt, I., Fernandez, M., Saura, E., Vergés, J., García-Castellanos, D., 2012. 3-D lithospheric structure and regional/residual Bouguer anomalies in the Arabia—Eurasia collision (Iran). Geophys. J. Int. 190 (3), 1311–1324. https://doi.org/10.1111/j.1365-246X.2012.05580.x.

Kaviani, A., Hatzfeld, D., Paul, A., Tatar, M., Priestley, K., 2009. Shear-wave splitting, lithospheric anisotropy, and mantle deformation beneath the Arabia–Eurasia collision zone in Iran. Earth Planet. Sci. Lett. 286 (3–4), 371–378. https://doi.org/10.1016/j.epsl.2009.07.003.

Kaviani, A., Mahmoodabadi, M., Rümpker, G., Pilia, S., Tatar, M., Nilfouroushan, F., Ali, M.Y., 2021. Mantle-flow diversion beneath the Iranian plateau induced by Zagros' lithospheric keel. Sci. Rep. 11 (1), 2848 https://doi.org/10.1038/s41598-021-81541-9.

Kaviani, A., Paul, A., Bourova, E., Hatzfeld, D., Pedersen, H., Mokhtari, M., 2007. A strong seismic velocity contrast in the shallow mantle across the Zagros collision zone (Iran). Geophys. J. Int. 171 (1), 399–410. https://doi.org/10.1111/j.1365-246X.2007.03535.x.

Khorrami, F., Vernant, P., Masson, F., Nilforoushan, F., Mousavi, Z., Nankali, H., Alijanzade, M., 2019. An up-to-date crustal deformation map of Iran using integrated campaign-mode and permanent GPS velocities. Geophys. J. Int. 217 (2), 832–843. https://doi.org/10.1093/gji/ggz045.

Levin, V., Park, J., 1998. Quasi-Love phases between Tonga and Hawaii: observations, simulations, and explanations. J. Geophys. Res.: Solid Earth 103 (B10), 24321–24331. https://doi.org/10.1029/98JB02342.

Levin, V., Park, J., Lucente, F.P., Margheriti, L., Pondrelli, S., 2007. End of subduction in northern Apennines confirmed by observations of quasi-Love waves from the great 2004 Sumatra-Andaman earthquake. Geophys. Res. Lett. 34 (4) https://doi.org/10.1029/2006GL028860.

Long, M.D., Becker, T.W., 2010. Mantle dynamics and seismic anisotropy. Earth Planet. Sci. Lett. 297 (3–4), 341–354. https://doi.org/10.1016/j.epsl.2010.06.036.

Lü, Y., Ni, S., Chen, L., Chen, Q.F., 2017. Pn tomography with Moho depth correction from eastern Europe to western China. J. Geophys. Res.: Solid Earth 122 (2), 1284–1301. https://doi.org/10.1002/2016JB013052.

Mahmoodabadi, M., Yaminifard, F., Tatar, M., Kaviani, A., Motaghi, K., 2019. Upper-mantle velocity structure beneath the Zagros collision zone, Central Iran and Alborz from nonlinear teleseismic tomography. Geophys. J. Int. 218 (1), 414–428. https://doi.org/10.1093/gji/ggz160.

Mahmoodabadi, M., Yaminifard, F., Tatar, M., Kaviani, A., 2020. Shear wave velocity structure of the upper-mantle beneath the northern Zagros collision zone revealed by nonlinear teleseismic tomography and Bayesian Monte-Carlo joint inversion of surface wave dispersion and teleseismic P-wave coda. Phys. Earth Planet. Inter. 300, 106444 https://doi.org/10.1016/j.pepi.2020.106444.

Margheriti, L., Lucente, F.P., Park, J., Pondrelli, S., Levin, V., Steckler, M.S., Salimbeni, S., 2014. Large-scale coherent anisotropy of upper mantle beneath the Italian peninsula comparing quasi-Love waves and SKS splitting. J. Geodyn. 82, 26–38. https://doi.org/10.1016/j.jog.2014.07.007.

Mohammadi, N., Rahimi, H., Gholami, A., Pachhai, S., Aoudia, A., 2022. Shear-wave velocity structure of upper mantle along the Zagros collision zone. Tectonophysics 837, 229444. https://doi.org/10.1016/j.tecto.2022.229444.

Mohammadi, E., Sodoudi, F., Kind, R., Rezapour, M., 2013. Presence of a layered lithosphere beneath the Zagros collision zone. Tectonophysics 608, 366–375. https://doi.org/10.1016/j.tecto.2013.09.017.

Motaghi, K., Shabanian, E., Kalvandi, F., 2017. Underplating along the northern portion of the Zagros suture zone, Iran. Geophys. J. Int. 210 (1), 375–389. https://doi.org/10.1093/gji/ggx168.

Motaghi, K., Tatar, M., Priestley, K., Romanelli, F., Doglioni, C., Panza, G.F., 2015. The deep structure of the Iranian Plateau. Gondwana Res. 28 (1), 407–418. https://doi.org/10.1016/j.gr.2014.04.009.

Motavalli-Anbaran, S.H., Zeyen, H., Brunet, M.F., Ardestani, V.E., 2011. Crustal and lithospheric structure of the Alborz Mountains, Iran, and surrounding areas from integrated geophysical modeling. Tectonics 30 (5). https://doi.org/10.1029/2011TC002934.

Movaghari, R., Doloei, G.J., 2020. 3-D crustal structure of the Iran plateau using phase velocity ambient noise tomography. Geophys. J. Int. 220 (3), 1555–1568. https://doi.org/10.1093/gji/ggz537.

Movaghari, R., JavanDoloei, G., Yang, Y., Tatar, M., Sadidkhouy, A., 2021. Crustal radial anisotropy of the Iran Plateau inferred from ambient noise tomography. J. Geophys. Res.: Solid Earth 126 (4), e2020JB020236. https://doi.org/10.1029/2020JB020236.

Namvaran, M., Tatar, M., Motavalli–Anbaran, S.H., 2020. Imaging the 2–D crust and upper mantle structure of the Iranian plateau resolved by potential field and seismic data. Phys. Earth Planet. Inter. 300, 106445 https://doi.org/10.1016/j.pepi.2020.106445.

Nissen-Meyer, T., van Driel, M., Stähler, S.C., Hosseini, K., Hempel, S., Auer, L., Fournier, A., 2014. AxiSEM: broadband 3-D seismic wavefields in axisymmetric media. Solid Earth 5 (1), 425–445. https://doi.org/10.5194/se-5-425-2014.

Park, J., 1993. The sensitivity of seismic free oscillations to upper mantle anisotropy 1. Zonal symmetry. J. Geophys. Res.: Solid Earth 98 (B11), 19933–19949. https://doi.org/10.1029/93JB02177.

Park, J., 1997. Free oscillations in an anisotropic earth: path-integral asymptotics. Geophys. J. Int. 129 (2), 399–411. https://doi.org/10.1111/j.1365-246X.1997.tb01591.x.

Park, J., Yu, Y., 1992. Anisotropy and coupled free oscillations: simplified models and surface wave observations. Geophys. J. Int. 110 (3), 401–420. https://doi.org/10.1111/j.1365-46X.1992.tb02082.x.

Paul, A., Hatzfeld, D., Kaviani, A., Tatar, M., Péquegnat, C., 2010. Seismic imaging of the lithospheric structure of the Zagros mountain belt (Iran). Geol. Soc., Lond., Spec. Publ. 330 (1), 5–18. https://doi.org/10.1144/SP330.2.

Paul, A., Kaviani, A., Hatzfeld, D., Vergne, J., Mokhtari, M., 2006. Seismological evidence for crustal-scale thrusting in the Zagros mountain belt (Iran). Geophys. J. Int. 166 (1), 227–237. https://doi.org/10.1111/j.1365-246X.2006.02920.x.

Pilia, S., Jackson, J.A., Hawkins, R., Kaviani, A., Ali, M.Y., 2020. The southern Zagros collisional orogen: new insights from transdimensional trees inversion of seismic noise. Geophys. Res. Lett. 47 (4), e2019GL086258 https://doi.org/10.1029/2019GL086258.

Priestley, K., McKenzie, D., Barron, J., Tatar, M., Debayle, E., 2012. The Zagros core: deformation of the continental lithospheric mantle. Geochem., Geophys., Geosystems 13 (11). https://doi.org/10.1029/2012GC004435.

Rahmani, M., Motaghi, K., Ghods, A., Sobouti, F., Talebian, M., Ai, Y., Chen, L., 2019. Deep velocity image of the north Zagros collision zone (Iran) from regional and teleseismic tomography. Geophys. J. Int. 219 (3), 1729–1740. https://doi.org/10.1093/gji/ggz393.

Rastgoo, M., Rahimi, H., Motaghi, K., Shabanian, E., Romanelli, F., Panza, G.F., 2018. Deep structure of the Alborz Mountains by joint inversion of P receiver functions and dispersion curves. Phys. Earth Planet. Inter. 277, 70–80. https://doi.org/10.1016/j.pepi.2018.01.011.

Rieger, D.M., Park, J., 2010. USArray observations of quasi-Love surface wave scattering: orienting anisotropy in the Cascadia plate boundary. J. Geophys. Res.: Solid Earth 115 (B5). https://doi.org/10.1029/2009JB006754.

Sadeghi-Bagherabadi, A., Margheriti, L., Aoudia, A., Sobouti, F., 2018b. Seismic anisotropy and its geodynamic implications in Iran, the easternmost part of the Tethyan Belt. Tectonics 37 (12), 4377–4395. https://doi.org/10.1029/2018TC005209.

Sadeghi-Bagherabadi, A., Sobouti, F., Ghods, A., Motaghi, K., Talebian, M., Chen, L., He, Y., 2018a. Upper mantle anisotropy and deformation beneath the major thrust-and-fold belts of Zagros and Alborz and the Iranian Plateau. Geophys. J. Int. 214 (3), 1913–1918. https://doi.org/10.1093/gji/ggy233.

Shad Manaman, N., Shomali, H., 2010. Upper mantle S-velocity structure and Moho depth variations across Zagros belt, Arabian–Eurasian plate boundary. Phys. Earth Planet. Inter. 180 (1–2), 92–103. https://doi.org/10.1016/j.pepi.2010.01.011.

Shad Manaman, N., Shomali, H., Koyi, H., 2011. New constraints on upper-mantle S-velocity structure and crustal thickness of the Iranian plateau using partitioned waveform inversion. Geophys. J. Int. 184 (1), 247–267. https://doi.org/10.1111/j.1365-246X.2010.04822.x.

Shomali, Z.H., Keshvari, F., Hassanzadeh, J., Mirzaei, N., 2011. Lithospheric structure beneath the Zagros collision zone resolved by non-linear teleseismic tomography. Geophys. J. Int. 187 (1), 394–406. https://doi.org/10.1111/j.1365-246X.2011.05150.x.

Veisi, M., Sobouti, F., Chevrot, S., Abbasi, M., Shabanian, E., 2021. Upper mantle structure under the Zagros collision zone; insights from 3D teleseismic P-wave tomography. Tectonophysics 819, 229106. https://doi.org/10.1016/j.tecto.2021.229106.

Wei, W., Zhao, D., Wei, F., Bai, X., Xu, J., 2019. Mantle dynamics of the eastern Mediterranean and Middle East: constraints from P-wave anisotropic tomography. Geochem., Geophys., Geosystems 20 (10), 4505–4530. https://doi.org/10.1029/2019GC008512.

Wu, Z., Chen, L., Talebian, M., Wang, X., Jiang, M., Ai, Y., Zhu, R., 2021. Lateral structural variation of the lithosphere-asthenosphere system in the northeastern eastern Iranian plateau and its tectonic implications. J. Geophys. Res.: Solid Earth 126 (1), e2020JB020256. https://doi.org/10.1029/2020JB020256.

Yu, Y., Park, J., 1993. Upper mantle anisotropy and coupled-mode long-period surface waves. Geophys. J. Int. 114 (3), 473–489. https://doi.org/10.1111/j.1365-246X.1993.tb06981.x.

Yu, Y., Park, J., Wu, F., 1995. Mantle anisotropy beneath the Tibetan Plateau: evidence from long-period surface waves. Phys. Earth Planet. Inter. 87 (3–4), 231–246. https://doi.org/10.1016/0031-9201(94)02971-D.